

# Imaging process and signal-to-noise ratio improvement of enhanced self-heterodyne synthetic aperture imaging lidar

Guo Zhang (张国)<sup>1,2</sup>, Jianfeng Sun (孙建锋)<sup>1,\*</sup>, Yu Zhou (周煜)<sup>1</sup>, Zhiyong Lu (卢智勇)<sup>1</sup>,  
Guangyuan Li (李光远)<sup>1,2</sup>, Guangyu Cai (蔡光宇)<sup>1,2</sup>, Mengmeng Xu (许蒙蒙)<sup>1,2</sup>,  
Bo Zhang (张波)<sup>1,2</sup>, Chenzhe Lao (劳陈哲)<sup>1,2</sup>, Hongyu He (贺红雨)<sup>1,2</sup>,  
and Liren Liu (刘立人)<sup>1</sup>

<sup>1</sup>Key Laboratory of Space Laser Communication and Detection Technology, Shanghai Institute of Optics and Fine Mechanics, Chinese Academy of Science, Shanghai 201800, China

<sup>2</sup>University of Chinese Academy of Sciences, Beijing 100049, China

\*Corresponding author: sunjianfeng@163.com

Received March 27, 2017; accepted June 16, 2017; posted online July 21, 2017

This Letter gives the general construction of an enhanced self-heterodyne synthetic aperture imaging lidar (SAIL) system, and proposes the principle of image processing. A point target is reconstructed in the enhanced self-heterodyne SAIL as well as in down-looking SAIL experiments, and the achieved imaging resolution of the enhanced self-heterodyne SAIL is analyzed. The signal-to-noise ratio (SNR) of the point target final image in the enhanced self-heterodyne SAIL is higher than that in the down-looking SAIL. The enhanced self-heterodyne SAIL can improve the SNR of the target image in far-distance imaging, with practicality.

OCIS codes: 280.3640, 280.6730, 100.2000, 100.3010, 030.1670.

doi: 10.3788/COL201715.102801.

Synthetic aperture imaging lidar (SAIL) originates from microwave synthetic aperture radar (SAR). In recent years, side-looking SAIL has demonstrated full two-dimensional (2D) SAIL imaging in the laboratory<sup>[1-7]</sup> and airborne<sup>[8,9]</sup>. There are many inherent defects in side-looking SAIL, such as small optical footprint, limited receiving aperture, need of a matched optical delay, and, in particular, susceptible suffering from the phase interferences of atmospheric turbulence and mechanical trembling in environments. To mitigate the limitations of the side-looking SAIL, a down-looking SAIL was proposed<sup>[10]</sup>. The down-looking SAIL is based on the key ideas of wavefront transformation of two coaxial and orthogonally polarized beams, and a receiver of self-heterodyne detection. The two coaxial and orthogonally polarized beams have the same transmitting and receiving path, thus, in the down-looking SAIL self-heterodynes the two beams could automatically compensate the phase error from atmospheric turbulence and unmodeled line-of-sight motion, and, in principle, no optical delay is needed. Meanwhile, the down-looking SAIL has a controllable and changeable size of the optical footprint, which, together with the associated imaging resolution, can be, manipulated on a large scale. The down-looking SAIL was demonstrated inside laboratory as well as outside under different atmospheric conditions<sup>[11-13]</sup>. The experiments of airborne down-looking SAIL is reported, and the laser power is 20 W for imaging the target at 3 km<sup>[14]</sup>. In fact, the laser power is limited and the laser with high power can damage the optical components in the down-looking SAIL transmitting system. The down-looking SAIL uses a self-heterodyne receiver to eliminate

phase error. However, the echo signal light is weak at far distances, resulting in low self-heterodyne efficiency and poor quality of the final image. Heterodyne detection is a method of obtaining quantum-limited reception in spectral ranges, and has many advantages in detecting weak signals<sup>[15,16]</sup>.

In this Letter, a enhanced self-heterodyne SAIL based on a down-looking SAIL, is proposed. This system self-heterodynes the two orthogonally polarized echo signals to produce a linear phase history in the orthogonal direction and a quadratic phase history in the travel direction during digital signal processing, and compresses the 2D data in the orthogonal direction by a Fourier transform. Further, it compresses using a match filter with a conjugate quadratic phase of the phase history in the travel direction to get the final target image. The enhanced self-heterodyne SAIL is practical in the far-distance imaging process. The enhanced self-heterodyne SAIL system uses a heterodyne receiver instead of a self-heterodyne receiver. The weak echo signal light interferes with the strong local oscillator, thus the signal-to-noise ratio (SNR) of the target image can be greatly improved.

The structure of the enhanced self-heterodyne SAIL system is illustrated in Fig. 1. The  $1 \times 2$  polarization-maintaining fiber coupler splits the laser generated by the laser source into two beams, a signal light, and a local oscillator. The signal light is amplified by an optical fiber amplifier and transmitted to the transmitter. The local oscillator is frequency-shifted using the acousto-optic frequency shifter. A rectangular stop near the cylindrical lenses is used to adjust the size of the inner beam.

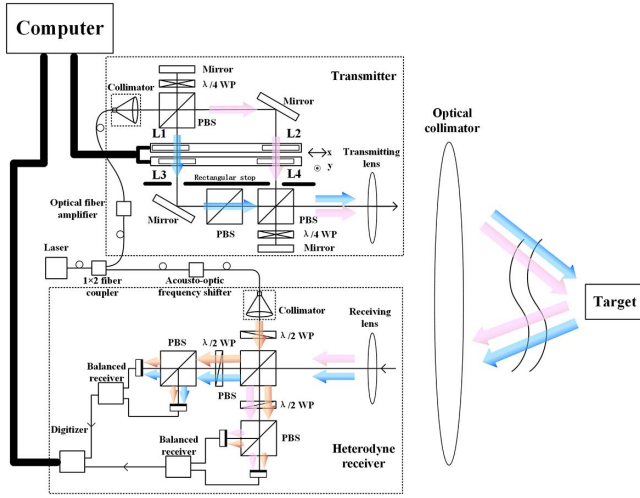


Fig. 1. Structure of the enhanced self-heterodyne SAIL system. PBS: polarizing beam splitter; WP: wave plate.

Plano-concave cylindrical lenses L1, L2, L3, and plano-convex cylindrical lens L4 are placed in the focal plane of the transmitting lens. The shift of L1 and L2 produce a linear phase in the orthogonal direction of travel<sup>[10]</sup>.

The configuration to translate the wavefront using cylindrical lenses L1, L2, L3, and L4 is shown in Fig. 2. Here, cylindrical lenses L1 and L2 move along the orthogonal direction of travel, two cylindrical lenses L3 and L4 move slowly along the direction of travel to produce a spatial quadratic phase history, whereas the target remains stationary.

Based on the structure of the enhanced self-heterodyne SAIL system, the inner optical fields of the two orthogonally polarized beams at the focal plane of the transmitting lens are<sup>[10-13]</sup>

$$e_H^0(x, y) = C \times \text{rect} \frac{x}{L_x} \text{rect} \frac{y}{L_y} \times \exp \left\{ -j \frac{\pi}{\lambda} \left[ \frac{(x - v_x t_f - S_b)^2}{R_1} + \frac{(y - v_y t_s)^2}{R_1} \right] \right\}, \quad (1)$$

$$e_V^0(x, y) = C \times \text{rect} \frac{x}{L_x} \text{rect} \frac{y}{L_y} \times \exp \left\{ -j \frac{\pi}{\lambda} \left[ \frac{(x + v_x t_f - S_b)^2}{R_1} - \frac{(y - v_y t_s)^2}{R_2} \right] \right\}, \quad (2)$$

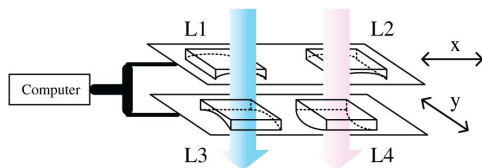


Fig. 2. Configuration to translate the wavefront using cylindrical lenses;  $x$  means the cylindrical lenses L1 and L2 are moving in the direction orthogonal to the direction of travel,  $y$  means the cylindrical lenses L3 and L4 are moving in the travel direction.

where  $C$  is the field amplitude of the signal light;  $\lambda$  is the wavelength of the signal light;  $R_1$  is the equivalent curvature radius of L1, L2, and L3;  $R_2$  is equivalent curvature radius of L4;  $L_x$  and  $L_y$  are the size of rectangular stops;  $t_f$  is the fast scanning time;  $t_s$  is the slow scanning time;  $v_x$  is the scanning velocity in the  $x$  (orthogonal) direction;  $v_y$  is the scanning velocity in the  $y$  (travel) direction;  $S_b$  is the distance between the center of the cylinder lens L1 (L2) and the corresponding propagation beam. Using an amplified transmission, the inner field is imaged onto the focal plane of the optical collimator with an amplification factor  $M$ , where  $M = f_c/f_t$ . The focal length of the optical collimator is  $f_c$ , whereas the focal length of the transmitting lens is  $f_t$ .

The echo signal light is collected from a point target at  $(x_p, y_p)$  by the receiving lens. Then, the optical fields of the two orthogonally polarized echo signal light on the receiving lens are<sup>[10]</sup>

$$e_H^r(x, y; x_p, y_p; t_f, t_s) = C_H \exp(j\varphi_H), \quad (3)$$

$$e_V^r(x, y; x_p, y_p; t_f, t_s) = C_V \exp(j\varphi_V), \quad (4)$$

$$C_H = C \times \text{rect} \frac{x_p}{ML_x} \text{rect} \frac{y_p}{ML_y}, \quad (5)$$

$$C_V = C \times \text{rect} \frac{x_p}{ML_x} \text{rect} \frac{y_p}{ML_y}, \quad (6)$$

$$\varphi_H = -\frac{\pi}{\lambda} \left[ \frac{(x_p - Mv_x t_f - MS_b)^2}{M^2 R_1} + \frac{(y_p - Mv_y t_s)^2}{M^2 R_1} \right] + \frac{\pi}{\lambda f_c} (x_p^2 + y_p^2) + \frac{\pi}{\lambda f_c} [(x - x_p)^2 + (y - y_p)^2] + \Delta\varphi_H, \quad (7)$$

$$\varphi_V = -\frac{\pi}{\lambda} \left[ \frac{(x_p + Mv_x t_f - MS_b)^2}{M^2 R_1} - \frac{(y_p - Mv_y t_s)^2}{M^2 R_2} \right] + \frac{\pi}{\lambda f_c} (x_p^2 + y_p^2) + \frac{\pi}{\lambda f_c} [(x - x_p)^2 + (y - y_p)^2] + \Delta\varphi_V. \quad (8)$$

The phase disturbance caused by the platform vibration and atmospheric turbulence during transmission and reception of the signal light are given by  $\Delta\varphi_H$  and  $\Delta\varphi_V$ , respectively. We assume that there is a uniform local oscillator with constant amplitude. The field of the local oscillator is given by

$$e_{LO} = C_{LO} \exp[j(\varphi_{LO} + \omega_{IF}t)], \quad (9)$$

where  $C_{LO}$  and  $\varphi_{LO}$  are the field amplitude and phase of the local oscillator and  $\omega_{IF}$  is the frequency shift between the signal light and local oscillator.

The echo signal light interferes with the local oscillator, and the resulting signal from the detector can be expressed by a radar equation for point target<sup>[10,15]</sup>. Hence, we have the signals from the two balanced receivers,

$$U_H(x_p, y_p; t_f, t_s) = C_{BD} C_{HLO} C_H \cos[\varphi_H + \Delta\varphi_F - (\varphi_{LO} + \omega_{IF}t)], \quad (10)$$

$$U_V(x_p, y_p; t_f, t_s) = C_{BD} C_{VLO} C_V \cos[\varphi_V + \Delta\varphi_F - (\varphi_{LO} + \omega_{IF}t)], \quad (11)$$

where  $C_{BD}$  is the photoelectric conversion factor, including all the system constants of integral and photoelectric conversion, also considering the signal light and local oscillator phase front alignment and beam spot size<sup>[47]</sup>.  $C_{HLO}$  and  $C_{VLO}$  are the field amplitudes of the local oscillator on the detector.  $\Delta\varphi_F$  is produced when the receiving lens focuses echo signal light onto the detector. During the digital signal processing, to self-heterodyne the two orthogonally polarized-echo signals,  $U_H(x_p, y_p; t_f, t_s)$  and  $U_V(x_p, y_p; t_f, t_s)$  are converted to complex form after the intermediate frequency  $\omega_{IF}$  is shifted, and  $U_H(x_p, y_p; t_f, t_s)$  is multiplied by the complex conjugate of  $U_V(x_p, y_p; t_f, t_s)$ . Thus, we have the 2D data

$$\begin{aligned} U(x_p, y_p; t_f, t_s) &= C_{BD}^2 C_{HLO} C_{VLO} C_V C_H \exp[j(\varphi_H - \varphi_V)] \\ &= C_{BD}^2 C_{HLO} C_{VLO} C_V C_H \\ &\quad \exp\left\{j\frac{\pi}{\lambda}\left[\frac{4(x_p - MS_b)v_x t_f}{MR_1} - \frac{(y_p - Mv_y t_s)^2}{M^2 R_3}\right]\right\}, \quad (12) \end{aligned}$$

where  $1/R_3 = 1/R_1 + 1/R_2$ . The two coaxial and orthogonally polarized signal lights have the same transmitting and receiving path, thus  $\Delta\varphi_H \approx \Delta\varphi_V$ , so the phase disturbance caused by the platform vibration and atmospheric turbulence can be compensated. During the imaging process, the 2D data  $U(x_p, y_p; t_f, t_s)$  is first compressed in the orthogonal direction using a Fourier transform. Then, the 2D data is compressed using a match filter with a conjugate quadratic phase of the phase history in the travel direction to get the target image<sup>[10]</sup>.

In our experiment, an optical collimator with a diameter of 600 mm and a focal length of 15 m is designed to simulate the far-distance situation due to the limitations of the laboratory site. A signal light with a wavelength of 1550 nm and a power of 27 dBm is used in the experiment. The local oscillator power is 3 dBm with a 10 kHz frequency shift. The focal length of each of the four cylindrical lenses is 150 mm. In addition, L1, L2, and L3 are plano-concave cylindrical lenses, and L4 is plano-convex cylindrical lens. The scanning velocity of the cylindrical lenses L1 and L2 is 5 mm/s, and the scanning time in the orthogonal direction is 1 s, so the scanning range in the orthogonal direction is 5 mm and the corresponding theoretical resolution is 0.29 mm. The scanning velocity of the cylindrical lenses L3 and L4 is 0.003 mm/s, and the scanning time in the travel direction is 1600 s, so the synthetic aperture length is 4.8 mm and the corresponding theoretical resolution is 0.30 mm<sup>[10]</sup>. The transmitting and receiving lenses have a diameter of 200 mm and a focal length of 1200 mm. The dimensions of the rectangular stop  $L_x$  and  $L_y$  are 7 mm. The balanced amplified photodetector PDB210C has a diameter of 3 mm. The point target is produced by covering the mirror and exposing only an area of 0.3 mm  $\times$  0.3 mm and placing it on the focal plane of the optical collimator.

The magnitude and phase distributions of the image focused in the orthogonal direction of travel using the Fourier transform are shown in Figs. 3(a) and 3(b). From Figs. 3(a) and 3(b), the final image resulting from the next focusing in the travel direction using match filtering is shown in Fig. 3(c). The resulting image has a full width at minimum of  $d_x \times d_y = 1.4 \text{ mm} \times 1.5 \text{ mm}$ , as shown in Figs. 3(d) and 3(e). The final resolution deviation from the theoretical calculation is mainly due to the nonlinearity of the lens shifting and the phase error of the inner optical fields. The phase error is caused by the cylindrical lens aberration and assembly position error.

Next, we change the output power of the optical fiber amplifier and image a 0.3 mm  $\times$  0.3 mm point target at

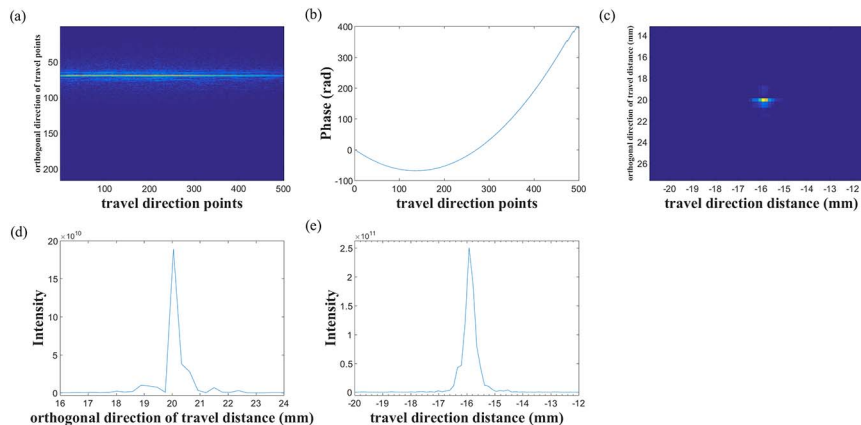


Fig. 3. (a) Magnitude and (b) phase distributions of the focused image in the orthogonal direction of travel and (c) a 2D image focused subsequently in the travel direction for a 0.3 mm  $\times$  0.3 mm point target. The distribution of the final image is (d) in orthogonal direction and (e) in the travel direction for a 0.3 mm  $\times$  0.3 mm point target.

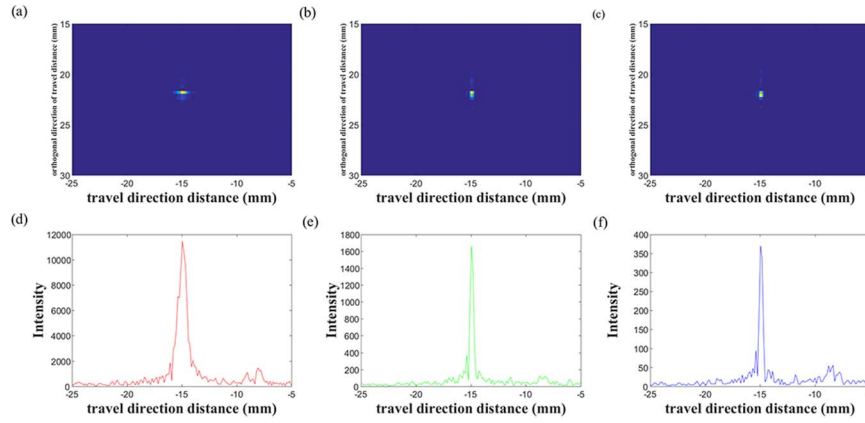


Fig. 4. (a), (b), and (c) are the final images for a  $0.3 \text{ mm} \times 0.3 \text{ mm}$  point target at output power of 15 mW, 2 mW, and  $750 \mu\text{W}$  of the optical fiber amplifier. (d), (e), and (f) are the distribution of the final image in the travel direction for a  $0.3 \text{ mm} \times 0.3 \text{ mm}$  point target at the output powers of 15 mW, 2 mW, and  $750 \mu\text{W}$  of the optical fiber amplifier.

different output powers. The final image for a  $0.3 \text{ mm} \times 0.3 \text{ mm}$  point target at output powers of 15 mW, 2 mW, and  $750 \mu\text{W}$  of the optical fiber amplifier are shown in Figs. 4(a)–4(c). The distribution of the final image in the travel direction for a  $0.3 \text{ mm} \times 0.3 \text{ mm}$  point target at output powers of 15 mW, 2 mW, and  $750 \mu\text{W}$  of the optical fiber amplifier are shown in Figs. 4(d)–4(f). We calculate the SNR of the point target final image in the travel direction to evaluate the final image quality. The standard deviation of the intensity of all points outside the full width at minimum is the intensity of noise  $\sigma_p$ . The maximum intensity in the full width at minimum subtracts the average intensity of all points outside the full width is the actual intensity of point target  $I_p$ .

Thus, the SNR of the point target final image is  $\text{SNR}_p = I_p/\sigma_p$ , and the values of  $\text{SNR}_p$  are shown in Table 1.

To compare the final image quality of the enhanced self-heterodyne SAIL system and down-looking SAIL, we do not change the transmitter. However, we change the heterodyne receiver to a self-heterodyne receiver by blocking the local oscillator and putting a half-wave plate behind the receiving lens. The structure of the self-heterodyne receiver in a down-looking SAIL is shown in Fig. 5.

Similarly, we change the output power of the optical fiber amplifier and image a  $0.3 \text{ mm} \times 0.3 \text{ mm}$  point target with the self-heterodyne receiver at different output powers. The final images for a  $0.3 \text{ mm} \times 0.3 \text{ mm}$  point target in a down-looking SAIL at the output powers of 15 mW, 2 mW, and  $750 \mu\text{W}$  of the optical fiber amplifier are shown in Figs. 6(a)–6(c). The distribution of the final image in the travel direction for a  $0.3 \text{ mm} \times 0.3 \text{ mm}$  point target in a down-looking SAIL at the output powers of 15 mW, 2 mW and,  $750 \mu\text{W}$  of the optical fiber amplifier are shown in Figs. 6(d)–6(f). The SNR of the point target final image in a down-looking SAIL are shown in Table 2.

With an increase in the output power, we can see that the point target final image becomes clear in Figs. 4 and 6,

**Table 1.** SNR of Point Target Final Image in Enhanced Self-heterodyne SAIL System

Output power of the optical fiber amplifier	Intensity of point target $I_p$	Intensity of noise $\sigma_p$	$\text{SNR}_p$
15 mW	11271	91	124
2 mW	1641	15	109
$750 \mu\text{W}$	364	6	61

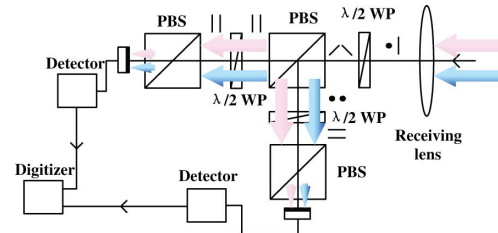


Fig. 5. Self-heterodyne receiver in the down-looking SAIL.

and the SNR of the point target final image has become higher in Tables 1 and 2, which correspond to the theory of the SNR of optical heterodyne detection<sup>[15]</sup>. Moreover, in the condition of the same output power, it is obvious that the point target final image in Fig. 4 is clearer than that in Fig. 6, and the SNR of the point target final image in Table 1 is higher than that in Table 2. It is clear that an enhanced self-heterodyne SAIL is more advantageous than a down-looking SAIL in far-distance imaging.

In conclusion, we propose the principle of an enhanced self-heterodyne SAIL system. We present SAIL experiments and achieved an imaging resolution of  $1.4 \text{ mm} \times 1.5 \text{ mm}$ . We compare the SNR of the point target final image in the enhanced self-heterodyne SAIL system and in the down-looking SAIL. The point target final image has a higher SNR and is clearer than that in the

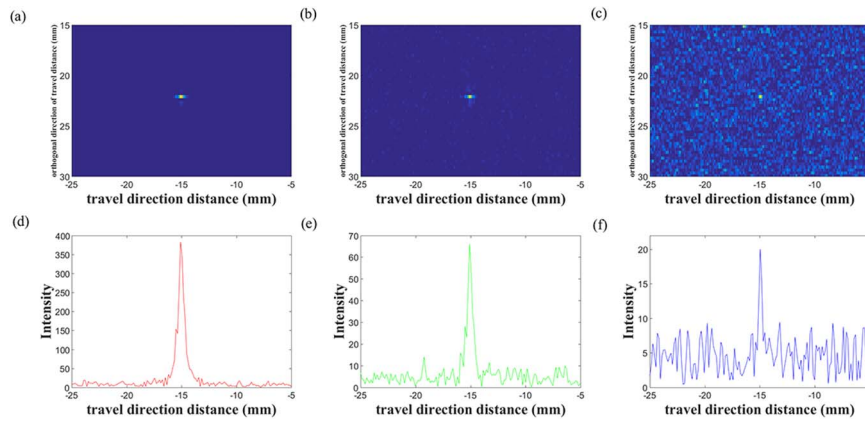


Fig. 6. (a), (b), and (c) are the final images for a  $0.3 \text{ mm} \times 0.3 \text{ mm}$  point target in the down-looking SAIL at the output powers of 15 mW, 2 mW, and  $750 \mu\text{W}$  of the optical fiber amplifier. (d), (e), and (f) are final images in the travel direction for a  $0.3 \text{ mm} \times 0.3 \text{ mm}$  point target in the down-looking SAIL at the output powers of 15 mW, 2 mW, and  $750 \mu\text{W}$  of the optical fiber amplifier.

**Table 2.** SNR of Point Target Final Image in Down-looking SAIL

Output power of the optical fiber amplifier	Intensity of point target $I_p$	Intensity of noise $\sigma_p$	$\text{SNR}_p$
15 mW	375.28	3.87	97
2 mW	61.59	2.37	26
$750 \mu\text{W}$	15.5	2.46	6

down-looking SAIL. The enhanced self-heterodyne SAIL greatly improves the SNR of the target final image, which is practical in far-distance imaging. In our experiment, the power of the local oscillator from the acousto-optic frequency shifter is 3 dBm, the balanced detector does not work in the quantum-limited condition. Thus, the SNR of the heterodyne receiver can be increased by increasing the local oscillator power. However, in this Letter, to compare the SNR of the final image in the enhanced self-heterodyne SAIL and the down-looking SAIL, we specifically image a point target. In our following work we plan to image a distributed target.

This work was supported by the National Natural Science Foundation of China (Nos. 61605226 and 61505233) and the Key Laboratory of Space Laser Communication and Detection Technology of Chinese Academy of Sciences.

## References

1. M. Bashkansky, R. L. Lucke, E. Funk, L. J. Rickard, and J. Reintjes, *Opt. Lett.* **27**, 1983 (2002).
2. S. M. Beck, J. R. Buck, W. F. Buell, R. P. Dickinson, D. A. Kozlowski, N. J. Marechal, and T. J. Wright, *Appl. Opt.* **44**, 7621 (2005).
3. M. Xing, L. Guo, Y. Tang, and B. Zang, *Infrared Laser Eng.* **38**, 290 (2009).
4. L. Liu, Y. Zhou, Y. Zhi, J. Sun, Y. Wu, Z. Luan, A. Yan, L. Wang, E. Dai, and W. Lu, *Acta. Opt. Sin.* **31**, 0900112 (2011).
5. J. Wu, Z. Yang, Z. Zhao, F. Li, D. Wang, Y. Tang, Y. Su, and N. Liang, *J. Infrared Millim. Waves.* **32**, 514 (2013).
6. Z. Zhao, J. Wu, Y. Su, N. Liang, and H. Duan, *Chin. Opt. Lett.* **12**, 091101 (2014).
7. Q. Xu, Z. Sun, J. Sun, Y. Zhou, Z. Lu, X. Ma, and L. Liu, *Chin. Opt. Lett.* **12**, 080301 (2014).
8. B. W. Krause, J. Buck, C. Ryan, D. Hwang, P. Kondratko, A. Malm, A. Gleason, and S. Ashby, in *OSA/CLEO* (2011), paper PDPB7.
9. K. Zhang, J. Pan, R. Wang, G. Li, N. Wang, and Y. Wu, *J. Radars* **6**, 1 (2017).
10. L. Liu, *Acta. Opt. Sin.* **32**, 0928002 (2012).
11. Z. Luan, J. Sun, Y. Zhou, L. Wang, M. Yang, and L. Liu, *Chin. Opt. Lett.* **12**, 111101 (2014).
12. Z. Lu, N. Zhang, J. Sun, Y. Zhou, Z. Luan, G. Cai, and L. Liu, *Chin. Opt. Lett.* **13**, 042801 (2015).
13. N. Zhang, Z. Lu, J. Sun, Y. Zhou, Z. Luan, Z. Sun, G. Li, and L. Liu, *Chin. Opt. Lett.* **13**, 091001 (2015).
14. Z. Lu, Y. Zhou, J. Sun, Z. Luan, L. Wang, Q. Xu, G. Li, G. Zhang, and L. Liu, *Chin. J. Lasers* **44**, 0110001 (2017).
15. D. Fink, *Appl. Opt.* **14**, 689 (1975).
16. O. E. DeLange, *IEEE Spectrum* **5**, 77 (1968).
17. S. C. Cohen, *Appl. Opt.* **14**, 1953 (1975).